Archives of Biochemistry and Biophysics 671 (2019) 35–41

Contents lists available at ScienceDirect

Archives of Biochemistry and Biophysics

journal homepage: www.elsevier.com/locate/yabbi

Probing direct interaction of oncomiR-21-3p with the tumor suppressor p53 by fluorescence, FRET and atomic force spectroscopy

Ilaria Moscetti, Salvatore Cannistraro*, Anna Rita Bizzarri

Biophysics and Nanoscience Centre, DEB, Università della Tuscia, Viterbo, Italy

ARTICLE INFO

Keywords:
miR-21
p53
Fluorescence quenching
FRET
AFS
oncomiR

ABSTRACT

miRNA-21-3p is overexpressed in a number of cancers and contributes to their development with a concomitant inhibition of the p53 onco-suppressive function. While a direct interaction of p53 with some miRNA precursors (namely pri-miRNAs and pre-miRNAs) was found, no interaction with mature micro RNA has been so far evidenced. It could therefore be very interesting to investigate if a direct interaction of miR-21-3p and p53 is occurring with possible impairment of the p53 onco-suppressive function. Fluorescence and Atomic Force Spectroscopy (AFS) were applied to study the interaction of p53 DNA Binding Domain (DBD) and miRNA-21-3p. Förster resonance energy transfer (FRET) was used to measure the distance between the DBD lone tryptophan (FRET donor) and a dye (FRET acceptor) bound to miRNA-21-3p. AFS and Fluorescence evidenced a direct interaction between miRNA-21-3p and DBD; with the formed complex being characterized by an affinity of 10^5 M, with a lifetime in the order of seconds. FRET allowed to determine an average distance of 4.0 nm between the DBD lone Trp146 and miRNA-21-3p; consistently with the involvement of the DBD L3 loop and/or the H1 helix in the complex formation, directly involved in the oligomerization and DNA binding. This may suggest that a functional inhibition of p53 could arise from its interaction with the oncogenic miRNA. Evidence of DBD-miRNA-21-3p complex formation may deserve some interest for inspiring novel therapeutic strategies.

1. Introduction

MicroRNAs (miRNAs) are small non-coding RNA of about 20 nucleotides that play a major role in the regulation of gene expression by controlling many crucial cell processes such as differentiation, development and apoptosis [1–4]. Some miRNAs may act as oncogenes (oncomiR), becoming overexpressed in many human malignancies [5–7]. Therefore, oncomiRs have emerged as promising diagnostic and prognostic biomarkers to assess tumor initiation, progression and response to treatment in cancer patients [8–12]. Among them, miRNA-21-3p (miR-21-3p) has been found to be overexpressed in a number of human cancer, including oral, ovarian and colorectal cancer [13–16]. It has been hypothesised that miR-21 contributes to cancer development by inhibiting apoptosis and stimulating proliferation, angiogenesis, and metastasis; thus it may deserve a remarkable interest as biomarker with diagnostic, prognostic and therapeutic value [17].

Interestingly, some miRNAs are able to control the network of the tumor suppressor p53, which indeed plays a pivotal role in the response to cellular stress signals, in cell cycle control and apoptosis and is impaired in almost all human cancers [18,19]. p53 and some of its oncogenic mutants have been found to bind to some miRNA precursors (namely pri-miRNAs and pre-miRNAs), especially in stressed conditions, with these interactions being involved in cancer development [20,21]. On the other hand, inhibition of p53 in cancer is caused by many different regulators [19]. such as ubiquitin ligases, which directly bind to p53, with the formation of a complex [22–24], and drive it to proteasomal degradation [25]. Interestingly, the simultaneous occurrence of both p53 functional impairment and miR-21-3p overexpression observed in some cancer types [13–15], led us to wonder if a direct interaction between them may be evidenced. In positive case, such an interaction might be correlated to the inhibition of p53 functional activity. In this connection, we studied the interaction *in vitro* between miR-21-3p and DBD, by exploiting both traditional and innovative nanotechnological spectroscopies, such Fluorescence, Förster Resonance Energy Transfer (FRET) and Atomic Force Spectroscopy (AFS). Fluorescence spectroscopy is a sensitive and powerful tool, operating in bulk, extensively used to investigate molecular interactions, which can be applied to systems bearing intrinsic or extrinsic fluorescence probes [26]. On the other hand, AFS is a single-molecule approach, operating without labelling, under near physiological conditions, and requiring a very little amount of interacting species [27]. It is particularly suited to investigate the unbinding kinetics of bio-complexes through the

* Corresponding author.
E-mail address: cannistr@unitus.it (S. Cannistraro).

https://doi.org/10.1016/j.abb.2019.05.026
Received 20 February 2019; Received in revised form 28 May 2019; Accepted 31 May 2019
Available online 08 June 2019
0003-9861/

measurement of molecular forces with picoNewton sensitivity [28,29]. These combined techniques, which have been previously exploited by some of the authors to study complexes involving p53 [23,30–32], allowed us to demonstrate the direct binding between DBD and miR-21-3p *in vitro*. They form a specific complex characterized by an affinity of about 10^5 M, with a lifetime in the order of seconds. In addition, careful FRET experiments evaluated an average distance of 4.0 nm between the lone Tryptophan of DBD, acting as the energy donor, and the miR-21-3p labelled with an appropriate acceptor dye. Accordingly, the most probable DBD regions involved in the interaction with miR-21-3p could be either the p53 DNA binding site or the oligomerization region; with both being crucial for the p53 oncosuppressive function. This unprecedented evidence of a direct interaction between DBD and miR-21-3p might suggest a possible impairment of p53 oncosuppressive function by this oncomiR. Such an information could be exploited for novel therapeutic strategies aimed at protecting the p53 function.

2. Materials and Methods

2.1. Materials

Recombinant human DNA binding domain (DBD) of p53 (residues 94–300) (23.4 kDa, purity > 90%, verified by HPLC and MS by the producer), containing a lone Tryptophan (Trp146), was purchased from Genscript (Piscataway, NJ, USA) by using the BacPower™ Guaranteed Bacterial Protein Expression Service.

Single stranded RNA oligonucleotide (ssRNA oligo) with the sequence of hsa-miR-21-3p (CAACACCAGUCGAUGGGCUGU) (6.7 kDa), (hereafter named miR-21-3p), ssRNA oligo of miR-21-3p modified at the 5′ end by adding an amino linker group (C6-NH2) (6.9 kDa) (hereafter NH2-miR-21-3p), and the same ssRNA oligo labelled with the Atto 390 fluorescent dye at the 5' end (7.2 kDa) (hereafter miR21-3p-Atto390) was purchased from Metabion (Planegg, Germany). The ssRNA oligo was purified by HPLC and verified by Mass spectroscopy by the producer. Phosphate-buffered saline solution 50 mM, pH 7.4 (hereafter PBS buffer) was prepared by using reagents from Sigma–Aldrich Co. (St Louis, MO, USA).

2.2. AFS experiments

Silicon nitride AFM tips (cantilever B, MSNL-10; Bruker Corporation), with a nominal spring constant, k_{nom}, of 0.02 N/m, were functionalized by covalently linking NH2-miR-21-3p (1.3 μM in PBS buffer) according to the procedure previously reported (Fig. 1A) [23]. Briefly, tips were cleaned in acetone for 10 min, dried with nitrogen and ultraviolet irradiated for 30 min. Then, they were incubated with a solution of 2% (v/v) 3-mercatopropyl-trimethoxysilane (Sigma–Aldrich Co.) in toluene (99.5%; Sigma–Aldrich Co.) for 2 h at room temperature and extensively washed with toluene. Subsequently, the silanized tips were incubated with a solution of 1 mM *N*-hydroxysuccinimide–polyethyleneglycol–maleimide (NHS-PEG-MAL, 3.4 kDa, N = 24, hereafter PEG) (Thermo Fisher Scientific, Waltham, MA, USA) in dimethyl sulfoxide (DMSO) (99.9%, Sigma–Aldrich Co.) for 3 h at room temperature. This PEG spacer contains maleimide (MAL), a thiol-reactive group at one end, to link silane molecules, and at the other an amino-reactive group (NHS), able to couple NH_2 groups. Then, tips were rinsed in DMSO to remove the unbound PEG. Successively, they were incubated with 10 μL of NH_2-miR-21-3p (1.3 μM) in PBS buffer overnight at 4 °C. Finally, the functionalized tips were gently rinsed with 10 mM PBS buffer and Milli-Q water.

2D-Aldehyde-functionalized glass surfaces, 1 cm^2 (PolyAn GmbH, Berlin, Germany), characterized by a thin silane layer able to covalently bind proteins via their exposed amino groups, were incubated with 50 μL of DBD-p53 (2 μM) in PBS buffer overnight at 4 °C, as shown in Fig. 1B. Then, the substrate was gently rinsed with PBS buffer and Milli-Q water. Finally, to passivate unreacted groups, both tips and substrates were incubated with 1 M ethanolamine hydrochloride pH 8.5 (GE Healthcare) for 30 min at room temperature and then rinsed with PBS buffer and Milli-Q water. Finally, samples were stored in PBS buffer at 4 °C.

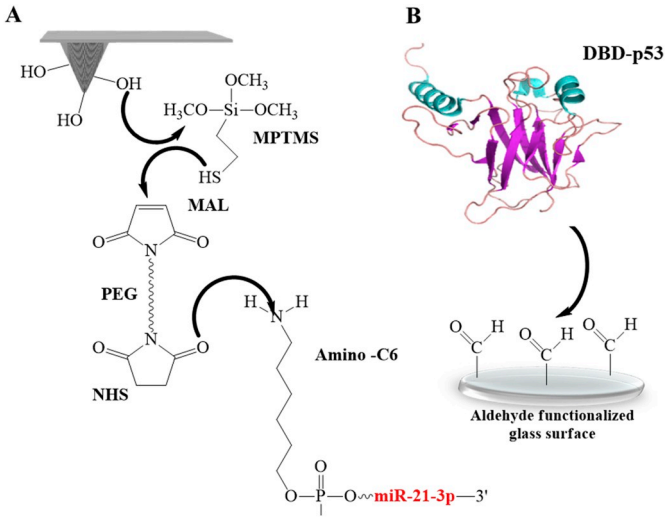

Fig. 1. Schematic representation of the surface chemistry used to covalently bind miR-21-3p (highlighted in red) and DBD to AFM tips and substrate, respectively. (**A**) The NH2-miR-21-3p was linked to the AFM tip through the -NH2 group, exposed at the 5'end of its Amino–C6 linker, after the tip functionalization with MPTMS and NHS-PEG-MAL cross-linker. (**B**) DBD was immobilized over the aldehyde-functionalized glass surface by randomly targeting amino groups of lysine residues exposed on the protein surface.

Unbinding force measurements were performed at room temperature with the Nanoscope IIIa/Multimode AFM (Veeco Instruments, Plainview, NY, USA) in PBS buffer. Force curves were acquired by using tips functionalized with NH_2-miR-21-3p, as previously described. A ramp size of 150 nm and an encounter time of 100 ms were set up. A relative trigger of 35 nm was used to limit at 0.7 nN the maximum contact force applied by the tip on the protein-functionalized substrate. Fig. 2 shows a representative approach–retraction cycle: at the beginning, the miR-21-3p-functionalized tip is moved toward the DBD-functionalized substrate (point 1). Then, the biomolecules jump to contact (point 2). A further pressure of the tip onto the substrate causes an upward deflection of the cantilever, as due to the electronic repulsion arising from the molecular orbital overlapping. Once the preset

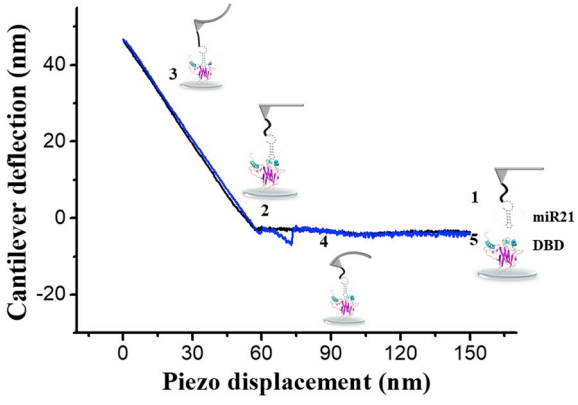

Fig. 2. A typical approach–retraction cycle of the miR-21-3p-functionalized tip over the DBD-functionalized substrate showing a specific unbinding event. (1) The tip moves toward the substrate. (2) The tip reaches the contact point. (3) A further pressure toward the substrate causes an upward deflection of the cantilever. (4) During the retraction, the cantilever bends downward due to the attractive interaction force of the miR-21-3p—DBD complex. (5) The cantilever jumps off, returning to its initial position.

maximum contact force value is reached, the approaching phase (black curve) of the cantilever is stopped (point 3) and the cantilever is retracted from the substrate. During this retraction phase (blue curve), adhesion forces and/or bonds formed during the contact phase cause the tip-bearing cantilever to bend downward, adhering to the substrate up to some distance beyond the initial contact point (point 4). As retraction continues, the spring force overcomes the interacting force and the cantilever jumps off, sharply returning to a noncontact position (point 5). Force curves were collected by approaching the functionalized tip to different points of the substrate at a constant velocity of 50 nm/s. The retraction velocity was varied from 50 to 4200 nm/s to match the selected values for the nominal loading rates, defined as the product of the cantilever k_{nom} by the tip pulling velocity and set in the range of 1–84 nN/s. The effective loading rates were then calculated from the product between the pulling velocity, v, and the spring constant of the entire system, k_{syst}, with this being determined from the slope of the retraction trace of the force curves immediately prior to the jump-off of an unbinding event, to take into account the effect of the molecules tied to the tip [33]. To obtain a reliable quantitative information with statistical significance, thousands of force curves were acquired at each loading rate. The exerted force, able to break the complex, called the unbinding force, F, was calculated by multiplying the cantilever deflection at the jump-off by its effective spring constant (k_{eff}), which was, in turn, determined by the non-destructive thermal noise method [34]. The force curves registered during the measurements showed different shapes. Therefore, we selected curves corresponding to specific unbinding events, being characterized, during the retraction phase, by sharp peaks with starting and ending points at zero deflection line, and by a nonlinear curved shape before the jump-off, which was related to the stretching features of the PEG linker (Fig. 2) [35]. In addition, the specificity of somewhat ambiguous unbinding events was also checked by using the 1/f noise approach [36,37]. Furthermore, a check of the specificity of the interaction was also performed by repeating the AFS experiments with a DBD-functionalized substrate incubated with 50 μL of NH2-miR-21-3p (1.3 μM) in PBS buffer overnight at 4 °C and with the same miR-21-3p-functionalized tip (hereafter referred to as blocking experiment).

2.3. Absorbance and fluorescence measurements

Absorbance spectra were recorded at room temperature by a double beam Jasco V-550UV/visible spectrophotometer by using 1-cm pathlength cuvettes and 1-nm bandwidth in the spectral region 220–750 nm, PBS buffer was used as reference.

Steady-state fluorescence measurements were performed by using a FluoroMax®-4 Spectrofluorometer (Horiba Scientific, Jobin Yvon), equipped with a thermostatted sample holder (Horiba) and a temperature bath. Samples were excited at 295 nm and fluorescence emission spectra were collected from 305 to 580 nm by using 1 nm increments and integration time of 0.50 s. A 2 nm bandpass width was used in both excitation and emission paths. Spectra were acquired in the signal to reference (S/R) mode to take into account for random lamp intensity fluctuations. Moreover, emission spectra were corrected for Raman contribution from the buffer. For each fluorescence experiment, ten measurements were performed on independently prepared samples by determining the average and the corresponding standard deviation. Spectra were analysed by using the FluorEssence software (Horiba Scientific).

Lifetime measurements were performed at room temperature with the time-correlated single photon counting method using FluoroMax®-4 Spectrofluorometer (Horiba Scientific, Jobin Yvon, France), operating at a repetition rate of 1 MHz and running in reverse mode. The apparatus was equipped with a pulsed nanosecond LED excitation head emitting at 295 nm (Horiba Scientific, Jobin Yvon, France) having a temporal width lower than 1 ns and a bandwidth of 4 nm. Detection was at 345 nm and the fluorescence lifetime data were acquired until the peak signal reached 10,000 counts. Time-resolved fluorescence decays were analysed by making use of the impulse response function (DAS6 software, Horiba Scientific, Jobin Yvon, France).

The function describing the intensity fluorescence decay was assumed to be a sum of exponentials and data were analysed by employing a non-linear least square analysis including deconvolution of the prompt from Horiba, JobinYvon: $I(t) = \sum_{i=1}^{n} a_i e^{(-t/\tau_i)}$ in which $I(t)$ is the time-dependent intensity, α_i is the pre-exponential factor representing fractional contribution to the time resolved decay of the i_{th} component with lifetime τ_i. The goodness of the fit was judged in term of both χ^2 value and weighted residuals. The fluorescence decay of DBD was found to be bi-exponential. The average fluorescence lifetime of Trp-214, $< \tau >$, was then calculated by: $<\tau> = \frac{\sum_{i=1}^{n} a_i \tau_i}{\sum_{i=1}^{n} a_i}$.

3. Results and discussions

3.1. AFS results

The interaction between DBD and miR-21-3p was investigated at the single-molecule level by applying AFS. Approach–retraction cycles were performed by using a NH2-miR-21-3p-functionalized tip and a DBD-conjugated substrate, prepared as described in the Materials and Methods section. Specific force curves were collected at five increasing loading rates. The unbinding forces were evaluated and cast into a histogram for each loading rate. In all the cases, a single mode distribution was obtained and the most probable unbinding force (F*) was extracted from the maximum of the peak of the corresponding histogram (Fig. 3A).

The recorded F* value was found to increase as far as higher loading rates were applied. The unbinding frequency, calculated as the ratio of the number of events corresponding to specific unbinding processes over the total recorded events, was around 33%. Blocking experiments provided a significant reduction (of more than 40%) of the unbinding events, witnessing the specificity of the DBD—miR-21-3p interaction. Since the molecular dissociation measured by AFS takes place under the application of an external force, the system is far from the thermodynamic equilibrium with a concomitant alteration of the energy profile. Therefore, to extract the kinetic and energy landscape parameters

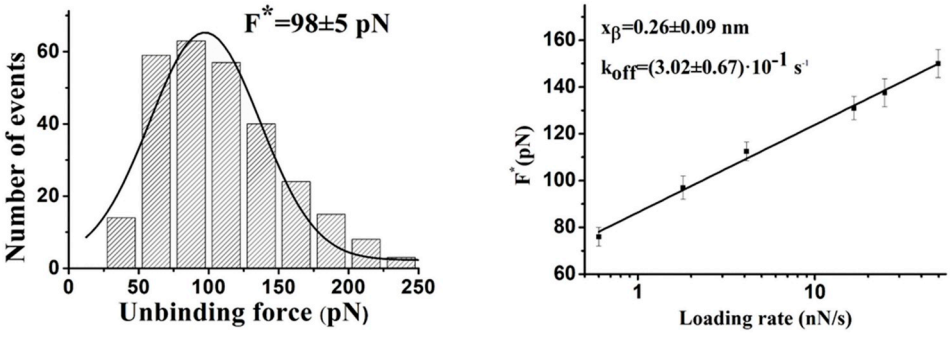

Fig. 3. (A) A representative histogram of the unbinding forces for the DBD—miR-21-3p complex from AFS measurements carried out at a loading rate of 3 nN/s. The most probable unbinding force value (F*) was determined from the maximum of the main peak of the histogram by fitting with a Gaussian function (black curve). (B) Plot of the most probable unbinding forces, F*, versus the logarithm of the loading rate for the DBD—miR-21-3p interaction. The solid line is the best fit of the experimental data by the Bell–Evans model (Equation (1)); the extracted values for the k_{off} and x_β parameters being reported.

at the equilibrium, we used the model developed by Bell and Evans [38,39], which predicts a linear dependence of the F* on the natural logarithm of the loading rate, r, as given by the following relationship:

$$F^* = \frac{k_B T}{x_\beta} \ln \frac{r\, x_\beta}{k_{off}\, k_B T} \quad (1)$$

where k_B is the Boltzmann constant, T is the absolute temperature, k_{off} is the dissociation rate constant, and x_β is the width of the energy barrier along the direction of the applied force. By plotting F* versus the logarithm of the effective loading rate (r), we observed a single linear trend indicative of a single energy barrier and a unique transition state of the reaction (Fig. 3B). By fitting these data with Equation (1), we found a k_{off} of $(3.0 \pm 0.7)\cdot 10^{-1}\,s^{-1}$ and a x_β of (0.26 ± 0.09) nm for the DBD—miR-21-3p complex, with these values being typical of specific biological complexes also involving p53 [40–42]. Furthermore, we calculated a lifetime τ ($\tau = 1/k_{off}$) of 3.3 s, which is much longer than that reported for unspecific RNA-protein interaction by using a similar approach [43,44].

To complete the kinetic characterization of the DBD—miR-21-3p complex at the single-molecule level, we estimated the association rate constant (k_{on}) according to the expression $k_{on} = N_A\, V_{eff}/t_{0.5}$, where N_A is the Avogadro's number, V_{eff} is the effective volume of a half-sphere with radius r_{eff} around the tip and $t_{0.5}$ is the time for the half-maximal binding probability, given by $t_{0.5} = 2r_{eff}/v$, where v is the pulling velocity [45,46]. Accordingly, a k_{on} of $\sim 10^4\,M^{-1}\,s^{-1}$ was obtained. The calculation of both the dissociation and association rate constants allowed us to determine the affinity constant $K_A = k_{on}/k_{off}$, of $\sim 10^5\,M$ for the DBD—miR-21-3p complex. The found value is similar to those reported for several ligand-receptor pairs, also involving p53 and it could indicate a transient character for the interaction [40,42].

3.2. Fluorescence quenching results

Fig. 4 shows the emission spectrum of DBD (1 μM in PBS buffer) excited at 295 nm at 298 K (black line). At this excitation wavelength, the single tryptophan residue (Trp146) of DBD still absorbs, while Tyr and Phe residues are not excited anymore. The spectrum shows a peak at about 345 nm (see the arrow), indicating that Trp146 is almost fully exposed to the solvent. The fluorescence emission of DBD becomes progressively reduced upon addition of increasing concentrations of miR-21-3p (colour lines in Fig. 4), with no significant wavelength shift of the emission peak; with this indicating that solvent exposition of Trp146 is not affected by the presence miR-21-3p, similarly to what reported for DNA and for an anticancer peptide, both binding to DBD [30,47].

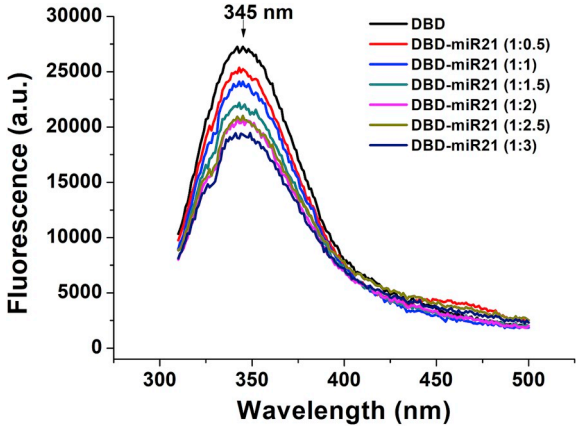

Fig. 4. Fluorescence emission spectra of DBD (1 μM in PBS buffer) alone (black line) and in presence of progressively higher concentrations of miR-21-3p (0.5–3 μM) (colour lines); The molar ratio of DBD:miR21 being reported in the inset. The peak of the DBD spectrum, at about 345 nm, is marked by an arrow. All the spectra were obtained by excitation at 295 nm and corrected for the Raman scattering of the buffer.

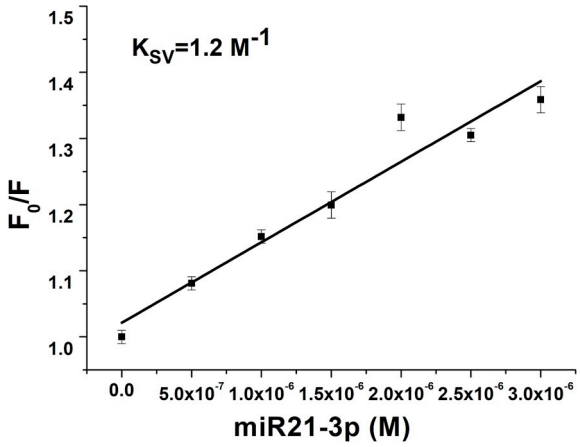

Fig. 5. Stern–Volmer plots of DBD—miR-21-3p. The fluorescence quenching (F_0/F) of DBD (1 μM in PBS buffer) plotted as a function of the miR-21-3p concentration (in the 0–3 μM range). Continuous black line is the linear fit by Eq. (2).

Fig. 5 shows the F_0/F ratio (squares) as a function of the miR-21-3p concentration, with F_0 and F being the fluorescence emission intensity at 345 nm of DBD in the absence and in the presence of miR-21-3p, respectively. The plot exhibits a linear trend which can be described by the well-known Stern–Volmer equation [26]:

$$\frac{F_0}{F} = 1 + k_q \tau_q [Q] = 1 + K_{SV}[Q] \quad (2)$$

where k_q is the bimolecular quenching constant (or quenching rate constant), K_{SV} is the Stern-Volmer quenching constant, [Q] is the concentration of the quencher (the miR-21-3p in our case) and τ_q is the average lifetime of the fluorophore (the lone Trp146 of DBD) in the absence of quencher, which was measured to be $(2.79 \pm 0.02)\cdot 10^{-9}$ s.

The K_{SV} value, determined from the slope of a linear fit of F_0/F data through Eq. (2) (see black lines in Fig. 5), was found to be $(1.2 \pm 0.2)\cdot 10^5\,M^{-1}$, while the corresponding bimolecular quenching constant, k_q, (evaluated from the relationship $k_q = K_{SV}/\tau_q$), was $k_q = (4.3 \pm 0.7)\cdot 10^{13} M^{-1} s^{-1}$. Notably, k_q is a much higher value than the diffusion-controlled quenching value, which typically is about $10^{10}\,M^{-1}\,s^{-1}$; with this indicating the occurrence of a static quenching mechanism [26]. To further support the nature of the quenching mechanism, we measured the lifetime of Trp146 after the addition of miR-21-3p at 1:1 molar ratio. We found a value of $(2.82 \pm 0.02)\cdot 10^{-9}$ s, which is almost the same of the lifetime of the DBD Trp146 alone; such an agreement supporting the occurrence of a static quenching mechanism, and then the formation of a stable complex between DBD and miR-21-3p in the ground state [26]. On such a basis, the Stern-Volmer constant K_{SV} can be interpreted as the affinity constant K_A of the complex formation. Interestingly, the K_A value determined by fluorescence in bulk ($K_A = 1.2\cdot 10^5\,M^{-1}$) is almost identical to that here obtained, at the single molecule level, by AFS ($K_A = 1\cdot 10^5\,M^{-1}$). Additionally, the evidence of a static quenching concomitantly with no wavelength shift of fluorescence peak at 345 nm, would suggest an allosteric mechanism at the basis of the quenching. In other words, binding of miR-21-3p may induce a conformational change on DBD, which, in turns, affecting the Trp146 fluorescence. In summary, fluorescence results demonstrated the formation of a specific and stable complex between DBD and the miR-21-3p, with an affinity K_A in the order of $10^5\,M^{-1}$.

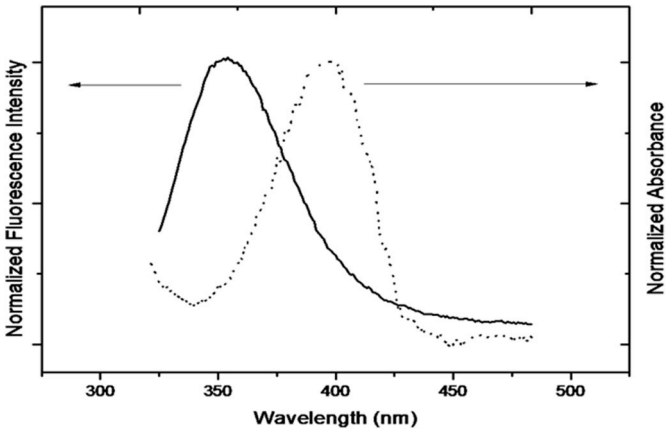

Fig. 6. Spectral overlap between the emission spectrum of the donor (Trp146 of p53-DBD) (solid line) and the absorption spectrum of the acceptor (miR-21-3p-Atto 390) (dashed line). Emission spectrum was obtained by exciting DBD in PBS buffer at 295 nm and was corrected for Raman scattering of the buffer. miR-21-3p-Atto 390 absorption was recorded in PBS buffer by using buffer as blank.

3.3. FRET results

To obtain additional information on the interaction between DBD and miR-21-3p, we applied the FRET technique which allows to estimate the distance between a donor (D) and an acceptor (A) from the D-A energy transfer efficiency (E_{FRET}). In our system, Trp146 of DBD is the donor (D), while Atto390 dye bound to miR-21-3p, is the acceptor (A). Indeed, they constitute an appropriate D-A couple for a FRET experiment since the emission spectrum of DBD reveals a high overlapping with the absorption spectrum of miR-21-3p-Atto 390 (Fig. 6). Accordingly, the D-A distance, R, is related to the energy transfer efficiency (E_{FRET}) through the expression [26]:

$$E_{FRET} = \frac{R_0^6}{R_0^6 + R^6} \tag{3}$$

where the Förster radius, R_0, is the D-A distance at which E_{FRET} is 0.5. R_0 (expressed in Å) can be calculated through the Förster formula [26]:

$$R_0^6 = 8.79\ 10^{-5} k^2 n^{-4} \varphi\ J \tag{4}$$

where k is the spatial orientation factor of the dipole, taken at 2/3, for a random orientation of both D and A; n is the refractive index of the medium, taken at 1.4; ϕ is the fluorescence quantum yield from D, taken at 0.07; finally, J is the overlap integral of the emission spectrum of D with the absorption spectrum of A. J was calculated from data shown in Fig. 6, by the expression:

$$J = \frac{\int_0^\infty F_D(\lambda)\varepsilon_A(\lambda)\lambda^4 d\lambda}{\int_0^\infty F_D(\lambda) d\lambda} \tag{5}$$

where $F_D(\lambda)$ is the fluorescence intensity of D at the wavelength λ and $\varepsilon_A(\lambda)$ is the molar absorption coefficient of the A at λ. From Eqs. (4) and (5), we found $R_0 = (2.5 \pm 0.1)$ nm, which is practically the same value obtained for the D-A couple Trp-Atto390 pair (2.5 nm) [48].

Three different methods were applied to evaluate E_{FRET}, and then to estimate the D-A distance: i) the quenching of fluorescence emission of D in the presence of A; ii) the enhancement of the fluorescence emission of A in the presence of D, and iii) the D lifetime variation in the presence of A.

Regarding the fluorescence emission quenching method, the E_{FRET} value can be determined from the equation [26]:

$$E_{FRET} = 1 - \frac{F_{DA}}{F_D} \tag{6}$$

where F_D and F_{DA} are the fluorescence emission intensities of D alone (DBD-miR—21-3p) and in the presence of A (DBD—miR-21-3p-Atto 390), respectively. Fig. 7A shows representative fluorescence emission spectra of DBD—miR-21-3p (red dashed line) and of DBD—miR-21-3p-Atto390 (black solid line), excited at 295 nm, at 1:1 molecular ratio. We note a further quenching of Trp146 of DBD in presence of miR21-3p when bound to Atto390, in comparison to the quenching of Trp146 of DBD as due to miR-21-3p (see Fig. 4); with this being indicative that an energy transfer from D to A is occurring. The fluorescence emission intensities, F_D and F_{DA}, at 345 nm, were determined from ten experiments performed on independently prepared samples. By Eq. (6), we obtained an average E_{FRET} value of $(6.5 \pm 0.3)\cdot 10^{-2}$, from which, through Eq. (5), an average D-A distance (R) of (3.9 ± 0.3) nm was derived.

Additionally, we evaluated E_{FRET} from the enhancement of the fluorescence emission of A, by the following expression [26]:

$$E_{FRET} = \left(\frac{F_{AD}}{F_A} - 1\right)\left(\frac{\varepsilon_A}{\varepsilon_D}\right) \tag{7}$$

where F_A and F_{AD} are the fluorescence emission intensities of A (miR-21-3p-Atto390) and of D (DBD—miR-21-3p-Atto390), respectively, while are ε_A and $\varepsilon_D = 1500\ M^{-1}cm^{-1}$ are the molar extinction coefficients of A ($\varepsilon_A = 2700\ M^{-1}cm^{-1}$) and of D ($\varepsilon_D = 1500\ M^{-1}cm^{-1}$) at the exciting wavelength of 295 nm [26,49,50]. Fig. 7B shows a representative spectrum of miR-21-3p-Atto390 emission (excited at 295 nm) (blue dashed curve) showing a peak at 463 nm, due to the Atto390 dye. This peak was found to be enhanced after the addition of miR-21-3p-Atto390 with DBD (1:1) (black solid curve), confirming thus

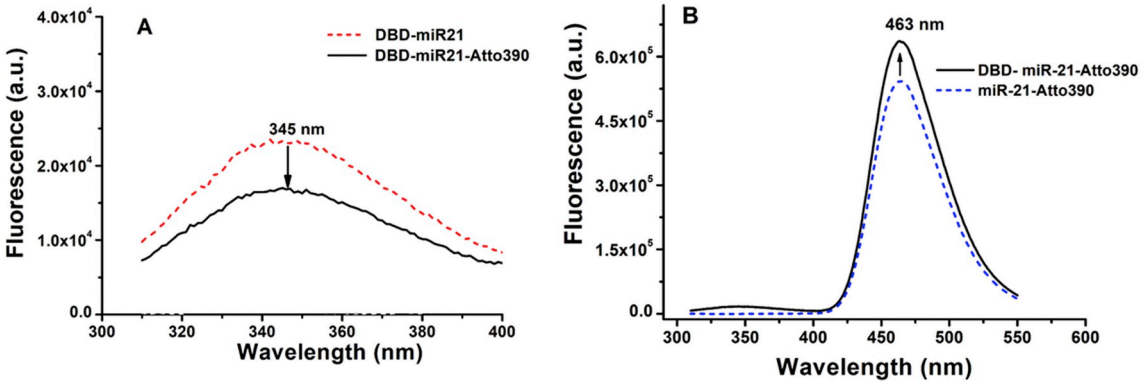

Fig. 7. A) Representative fluorescence emission spectra of DBD—miR21-3p (black solid line) and of DBD—miR-21-3p-Atto390 (red dashed line); both the spectra having been obtained at a concentration of 1 μM with a 1:1 molar ratio between DBD and miR21-3p or miR21-3p-Atto390. B) Representative fluorescence emission spectra of miR-21-3p-Atto390 (blue dashed line) at a concentration of 1 μM and of DBD—miR-21-3p-Atto390 (black solid line), both of them at a concentration of 1 μM, with a 1:1 molar ratio. All the spectra were excited at 295 nm and corrected for the Raman scattering of the buffer.

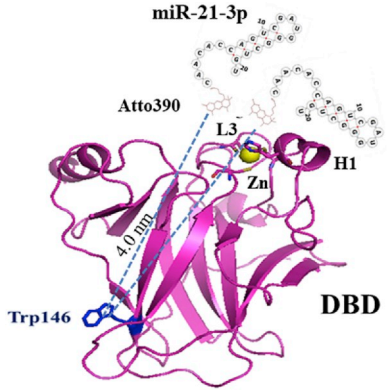

Fig. 8. Schematic representation of the most probable DBD—miR-21-3p-Atto390 interacting regions. The distance between the Atto390, bound to miR-21-3p at the 5′ end, and the center of the aromatic rings of Trp146 is indicated (blue dashed lines) for the two models.

the energy transfer from D to A. Upon determining F_A and F_{AD}, Eqs. (3) and (5) provide the D-A distance (R). From measurements of ten independently prepared samples, a value R of (3.9 ± 0.4 nm) nm was obtained. This value is in a very good agreement with that obtained by the donor fluorescence quenching method.

Finally, D lifetime variation method was used to calculate E_{FRET} through the equation [26]:

$$E_{FRET} = 1 - \frac{<\tau_{DA}>}{<\tau_D>} \quad (8)$$

where $<\tau_{DA}>$ and $<\tau_D>$ are the average D lifetime in the presence and absence of A, respectively. As previously reported, for the donor DBD—miR-21-3p, a lifetime of $<\tau_D> = (2.82 \pm 0.02)\cdot10^{-9}$ s was obtained, while for DBD—miR-21-3p-Atto 390, (i.e. D in the presence of A), we found a lower lifetime ($<\tau_{DA}> = (2.68 \pm 0.02)\cdot10^{-9}$ s); such a reduction being indicative of the occurrence of FRET in the DBD—miR-21-3p-Atto390 system. Accordingly, from Eqs. (3) and (8), we extracted an average D-A distance of 4.1 ± 0.1 nm. The slightly higher D-A distance, with respect to that evaluated by the two other methods, could be consistent with an overestimation of FRET efficiency in the latter cases; with this suggesting a small contribution from static quenching [26]. From the values obtained from three different FRET-based approaches, a weighted average D-A distance of (4.0 ± 0.1)nm, was evaluated.

The average DA distance of about 4.0 nm could be used to predict the localization of the most probable interaction regions between miR-21-3p and DBD. By screening the possible arrangements of miR-21-3p with respect to DBD, consistently with the evaluated distance between the dye bound to miR-21-3p with respect to Trp146, we could propose two possible models for the complex, which are shown in Fig. 8. We found that the interaction region of miR-21-3p with DBD is substantially the same in both cases. Concerning the DBD, we identified two putative regions involved in the binding: the H1 helix and the L3 loop. Notably, both these regions are close to the coordination of the Zn ion, which is devoted to the DNA binding process. Furthermore, the H1 helix is responsible for the DBD dimerization [51], while the L3 loop interacts with the minor groove of DNA [52]. In this context, we may speculate about a possible role played by miR-21-3p in the impairment of the p53 DNA binding function or in the oligomerization of p53; with both actions being susceptible to inhibit the p53 onco-suppressive function.

4. Conclusions

A molecular interaction between the oncogenic miR-21-3p and the major tumor suppressor p53 was disclosed *in vitro* by means of two complementary approaches, AFS and Fluorescence spectroscopy, working at the single molecule level and in bulk, respectively. We found the formation of a specific complex with an affinity of about 10^5 M and a lifetime in the order of seconds. Careful FRET measurements provided an estimation of a distance of about 4.0 nm between the intrinsic Trp146 of DBD and the acceptor dye bound to miR-21-3p. Such an information allowed to propose two possible topological configurations for the complex, elucidating two possible binding regions within the DBD. In particular, DBD could interact with miR-21-3p through the H1 helix, directly involved in the DBD oligomerization, and through the L3 loop which binds to the minor groove of DNA. Accordingly, it could be speculated about a possible role played by miR-21-3p in the impairment of the p53 DNA binding function and/or in the oligomerization of p53; with both actions being susceptible to inhibit the p53 onco-suppressive function. These unprecedented findings shine a new light on the interplay between p53 and oncogenic mature miRNAs, in addition to the well-known interaction of p53 with some miRNA precursors, and could inspire the development of new cancer therapies aimed at protecting the p53 function.

Acknowledgments

We thank the Italian Association for Cancer Research (AIRC) for financial support (Grant IG15866 to SC).

References

[1] D.P. Bartel, R. Lee, R. Feinbaum, MicroRNAs: genomics, biogenesis, mechanism, and function genomics: the miRNA genes, Cell 116 (2004) 281–297.
[2] L. He, G.J. Hannon, MicroRNAs: small RNAs with a big role in gene regulation, Nat. Rev. Genet. 5 (2004) 522.
[3] L. Macfarlane, P.R. Murphy, MicroRNA: Biogenesis, Function and Role in Cancer, (2010), pp. 537–561.
[4] F. Wahid, A. Shehzad, T. Khan, Y.Y. Kim, MicroRNAs: synthesis, mechanism, function, and recent clinical trials, Biochim. Biophys. Acta Mol. Cell Res. 1803 (2010) 1231–1243 https://doi.org/10.1016/j.bbamcr.2010.06.013.
[5] G.A. Calin, C.M. Croce, MicroRNA signatures in human cancers, Nat. Rev. Canc. 6 (2006) 857.
[6] F. Calore, F. Lovat, M. Garofalo, Non-coding RNAs and cancer, Int. J. Mol. Sci. 14 (2013), https://doi.org/10.3390/ijms140817085.
[7] A.A. Svoronos, D.M. Engelman, F.J. Slack, OncomiR or tumor suppressor? The duplicity of MicroRNAs in cancer, Cancer Res. 76 (2016) 3666–3670, https://doi.org/10.1158/0008-5472.CAN-16-0359.
[8] C. Corcoran, A.M. Friel, M.J. Duffy, J. Crown, L.O. Driscoll, Intracellular and extracellular MicroRNAs in breast cancer, Clin. Chem. 57 (2011) 18–32, https://doi.org/10.1373/clinchem.2010.150730.
[9] R. Garzon, G.A. Calin, C.M. Croce, MicroRNAs in cancer, Annu. Rev. Med. 60 (2009) 167–179, https://doi.org/10.1146/annurev.med.59.053006.104707.
[10] K. Ruan, X. Fang, G. Ouyang, MicroRNAs: novel regulators in the hallmarks of human cancer, Cancer Lett. 285 (2009) 116–126 https://doi.org/10.1016/j.canlet.2009.04.031.
[11] E. van Rooij, S. Kauppinen, Development of microRNA therapeutics is coming of age, EMBO Mol. Med. 6 (2014) 851 LP–864, https://doi.org/10.15252/emmm.201100899.
[12] K.B. Reddy, MicroRNA (miRNA) in cancer, Cancer Cell Int. 15 (2015) 38, https://doi.org/10.1186/s12935-015-0185-1.
[13] P.M. Báez-Vega, I.M. Echevarría Vargas, F. Valiyeva, J. Encarnación-Rosado, A. Roman, J. Flores, M.J. Marcos-Martínez, P.E. Vivas-Mejía, Targeting miR-21-3p inhibits proliferation and invasion of ovarian cancer cells, Oncotarget 7 (2016) 36321–36337, https://doi.org/10.18632/oncotarget.9216.
[14] K. Hasáková, J. Bilcikova, M. Vician, R. Reis, Z. Michal, I. Herichova, Gender-dependent Expression of Leading and Passenger Strand of miR-21 and miR-16 in Human Colorectal Cancer and Adjacent Colonic Tissues, (2017).
[15] O. Peralta-Zaragoza, J. Deas, A. Meneses-Acosta, F. De la O-Gómez, G. Fernández-Tilapa, C. Gómez-Cerón, O. Benítez-Boijseauneau, A. Burguete-García, K. Torres-Poveda, V.H. Bermúdez-Morales, V. Madrid-Marina, M. Rodríguez-Dorantes, A. Hidalgo-Miranda, C. Pérez-Plasencia, Relevance of miR-21 in regulation of tumor suppressor gene PTEN in human cervical cancer cells, BMC Canc. 16 (2016) 215, https://doi.org/10.1186/s12885-016-2231-3.
[16] H.-H. Tseng, Y.K. Tseng, J.-J. You, B.H. Kang, T.H. Wang, C.-M. Yang, H.C. Chen, H.H. Liou, P.F. Liu, L.P. Ger, K.W. Tsa, Next-generation sequencing for microRNA profiling: MicroRNA-21-3p promotes oral cancer metastasis, Anticancer Res. 37 (2017) 1059–1066.
[17] I. Negoi, S. Hostiuc, M. Sartelli, R.I. Negoi, M. Beuran, MicroRNA-21 as a prognostic biomarker in patients with pancreatic cancer – a systematic review and meta-analysis, Am. J. Surg. 214 (2017) 515–524 https://doi.org/10.1016/j.amjsurg.2017.03.049.

[18] J. Liu, C. Zhang, Y. Zhao, Z. Feng, MicroRNA Control of p53, 14 (2017) 7–14, https://doi.org/10.1002/jcb.25609.
[19] D. Lane, A. Levine, p53 Research: the past thirty years and the next thirty years, Cold Spring Harbor Perspect. Biol. 2 (2010), https://doi.org/10.1101/cshperspect.a000893 a000893–a000893.
[20] A. Gurtner, E. Falcone, F. Garibaldi, G. Piaggio, Dysregulation of microRNA biogenesis in cancer: the impact of mutant p53 on Drosha complex activity, J. Exp. Clin. Cancer Res. 35 (2016) 45, https://doi.org/10.1186/s13046-016-0319-x.
[21] H.I. Suzuki, K. Yamagata, K. Sugimoto, T. Iwamoto, S. Kato, K. Miyazono, Modulation of microRNA processing by p53, Nature 460 (2009) 529.
[22] I. Moscetti, E. Teveroni, F. Moretti, A.R. Bizzarri, S. Cannistraro, MDM2–MDM4 molecular interaction investigated by atomic force spectroscopy and surface plasmon resonance, Int. J. Nanomed. 11 (2016), https://doi.org/10.2147/IJN.S114705.
[23] I. Moscetti, A.R. Bizzarri, S. Cannistraro, Imaging and kinetics of the bimolecular complex formed by the tumor suppressor p53 with ubiquitin ligase COP1 as studied by atomic force microscopy and surface plasmon resonance, Int. J. Nanomed. 13 (2018), https://doi.org/10.2147/IJN.S152214.
[24] P.J. Paul, D. Raghu, A.-L. Chan, T. Gulati, L. Lambeth, E. Takano, M.J. Herold, J. Hagekyriakou, R.L. Vessella, C. Fedele, M. Shackleton, E.D. Williams, S. Fox, S. Williams, S. Haupt, C. Gamell, Y. Haupt, Restoration of tumor suppression in prostate cancer by targeting the E3 ligase E6AP, Oncogene 35 (2016) 6235.
[25] S. Sane, K. Rezvani, Essential roles of E3 ubiquitin ligases in p53 regulation, Int. J. Mol. Sci. 18 (2017), https://doi.org/10.3390/ijms18020442.
[26] J.R. Lakowicz, Principles of Fluorescence Spectroscopy, third ed., Springer US, 2006.
[27] P. Hinterdorfer, Y.F. Dufrêne, Detection and Localization of Single Molecular Recognition Events Using Atomic Force Microscopy, (2006), p. 3, https://doi.org/10.1038/NMETH871.
[28] A.R. Bizzarri, S. Cannistraro, The application of atomic force spectroscopy to the study of biological complexes undergoing a biorecognition process, Chem. Soc. Rev. 39 (2010) 734–749, https://doi.org/10.1039/b811426a.
[29] F.A. Carvalho, S. Connell, G. Miltenberger-Miltenyi, S.V. Pereira, A. Tavares, R.A.S. Ariëns, N.C. Santos, Atomic force microscopy-based molecular recognition of a fibrinogen receptor on human erythrocytes, ACS Nano 4 (2010) 4609–4620, https://doi.org/10.1021/nn1009648.
[30] A.R. Bizzarri, I. Moscetti, S. Cannistraro, BBA - general Subjects Interaction of the anticancer p28 peptide with p53-DBD as studied by fluorescence, FRET, docking and MD simulations, BBA Gener. Subj. 1863 (2019) 342–350, https://doi.org/10.1016/j.bbagen.2018.11.003.
[31] A.R. Bizzarri, S. Santini, E. Coppari, M. Bucciantini, S. Di Agostino, T. Yamada, C.W.C.W. Beattie, S. Cannistraro, Interaction of an anticancer peptide fragment of azurin with p53 and its isolated domains studied by atomic force spectroscopy, Int. J. Nanomed. 6 (2011) 3011–3019, https://doi.org/10.2147/IJN.S26155.
[32] S. Signorelli, S. Santini, T. Yamada, A.R. Bizzarri, C.W.C.W. Beattie, S. Cannistraro, Binding of amphipathic cell penetrating peptide p28 to wild type and mutated p53 as studied by Raman, Atom. Force Surf. Plasmon Reson. Spectrosc. 1861 (2017) 910–921, https://doi.org/10.1016/j.bbagen.2017.01.022.
[33] C. Friedsam, A.K. Wehle, F.K. hner, H.E. Gaub, I., Dynamic single-molecule force spectroscopy: bond rupture analysis with variable spacer length, J. Phys. Condens. Matter 15 (2003) S1709–S1723, https://doi.org/10.1088/0953-8984/15/18/305.
[34] J.L. Hutter, J. Bechhoefer, Calibration of atomic-force microscope tips, Rev. Sci. Instrum. 64 (1993) 1868, https://doi.org/10.1063/1.1143970.
[35] F. Kienberger, A. Ebner, H.J. Gruber, P. Hinterdorfer, F. Kienberger, A. Ebner, P. Hinterdorfer, Molecular Recognition Imaging and Force Spectroscopy of Single Biomolecules Molecular Recognition Imaging and Force Spectroscopy of Single Biomolecules, (2006), https://doi.org/10.1021/ar050084m.
[36] A.R. Bizzarri, S. Cannistraro, 1/fα noise in the dynamic force spectroscopy curves signals the occurrence of biorecognition, Phys. Rev. Lett. 110 (2013), https://doi.org/10.1103/PhysRevLett.110.048104.
[37] A.R. Bizzarri, S. Cannistraro, Antigen-antibody biorecognition events as discriminated by noise analysis of force spectroscopy curves, Nanotechnology 25 (2014) 335102, https://doi.org/10.1088/0957-4484/25/33/335102.
[38] G.I. Bell, Models for the specific adhesion of cells to cells, Science (New York, N.Y.) 200 (1978) 618–627.
[39] E. Evans, K. Ritchie, Dynamic strength of molecular adhesion bonds, Biophys. J. 72 (1997) 1541–1555, https://doi.org/10.1016/S0006-3495(97)78802-7.
[40] A.R. Bizzarri, S. Cannistraro, Atomic force spectroscopy in biological complex formation: strategies and perspectives, J. Phys. Chem. B 113 (2009) 16449–16464, https://doi.org/10.1021/Jp902421r.
[41] G. Funari, F. Domenici, L. Nardinocchi, R. Puca, G. D'Orazi, A.R. Bizzarri, S. Cannistraro, Interaction of p53 with Mdm2 and azurin as studied by atomic force spectroscopy, J. Mol. Recognit. 23 (2010) 343–351, https://doi.org/10.1002/jmr.999.
[42] I.M.A. Nooren, J.M. Thornton, Diversity of protein-protein interactions, EMBO J. 22 (2003) 3486–3492, https://doi.org/10.1093/emboj/cdg359.
[43] A. Fuhrmann, J.C. Schoening, D. Anselmetti, D. Staiger, R. Ros, Quantitative analysis of single-molecule RNA-protein interaction, Biophys. J. 96 (2009) 5030–5039, https://doi.org/10.1016/j.bpj.2009.03.022.
[44] J. Živković, L. Janssen, F. Alvarado, S. Speller, H.A. Heus, Force spectroscopy of Rev-peptide–RRE interaction from HIV-1, Soft Matter 8 (2012) 2103–2109, https://doi.org/10.1039/C1SM06563G.
[45] M. Taranta, A.R. Bizzarri, S. Cannistraro, Probing the interaction between p53 and the bacterial protein azurin by single molecule force spectroscopy, J. Mol. Recognit. 21 (2008) 63–70, https://doi.org/10.1002/jmr.869.
[46] E. Coppari, T. Yamada, A.R. Bizzarri, C.W. Beattie, S. Cannistraro, A nanotechnological, molecular-modeling, and immunological approach to study the interaction of the anti-tumorigenic peptide p28 with the p53 family of proteins, Int. J. Nanomed. 9 (2014) 1799–1813, https://doi.org/10.2147/IJN.S58465.
[47] Y. Cho, S. Gorina, P.D. Jeffrey, N.P. Pavletich, Crystal structure of a p53 tumor suppressor-DNA complex: understanding tumorigenic mutations, Science (New York, N.Y.). 265 (1994) 346–355, https://doi.org/10.1126/science.8023157.
[48] G. Zauner, E. Lonardi, L. Bubacco, T.J. Aartsma, Tryptophan-to-Dye Fluorescence Energy Transfer Applied to Oxygen Sensing by Using Type-3 Copper Proteins, (2007), pp. 7085–7090, https://doi.org/10.1002/chem.200601806.
[49] S. Santini, A.R. Bizzarri, S. Cannistraro, Revisitation of FRET methods to measure intraprotein distances in human serum albumin, J. Lumin. 179 (2016) 322–327, https://doi.org/10.1016/j.jlumin.2016.07.029.
[50] N.H.I. Medintz, FRET – Förster Resonance Energy Transfer from Theory to Applications, Wiley-VCHVerlag, Weinheim, 2014https://doi.org/10.1002/9783527656028.ch03.
[51] A.C. Joerger, C.R. Fersht, Structural biology of the tumor suppressor p53, Annu. Rev. Biochem. 77 (2008) 557–582, https://doi.org/10.1146/annurev.biochem.77.060806.091238.
[52] S.-W.W. Chi, S.-H.H. Lee, D.-H.H. Kim, M.-J.J. Ahn, J.-S.S. Kim, J.-Y.Y. Woo, T. Torizawa, M. Kainosho, K.-H.H. Han, Structural details on mdm2-p53 interaction, J. Biol. Chem. 280 (2005) 38795–38802, https://doi.org/10.1074/jbc.M508578200.